Progress In Electromagnetics Research, Vol. 127, 351–370, 2012

THE "SLOPE" EFFECT OF COHERENT TRANSPONDER IN InSAR DEM

Q.-F. Liu*, S.-Q. Xing, X.-S. Wang, J. Dong, D.-H. Dai, and Y.-Z. Li

School of Electronic Science and Engineering, National University of Defense Technology, Changsha 410073, China

Abstract—Although a Coherent Transponder (CT) is widely utilized in the field of Synthetic Aperture Radar (SAR), its Digital Elevation Model (DEM) has not yet been well studied for Interferometry SAR (InSAR). Based on the fact that the interferometry phase is a constant for CT with single transmit antenna, this paper mainly focuses on InSAR DEM induced by CT. The decorrelation effect in the intersection region of CT and natural terrain is researched in detail to support the analysis of CT's phase-unwrapping. The most important property, which makes DEM of CT unique, is found to be the "slope" effect. The incline angle of "main slope" of DEM is verified to be determined only by the depression angle of InSAR baseline, whereas the incline angles of the "subordinate slopes" are affected by all the geometric parameters of InSAR baseline. Finally, all the incline angles are independent of CT's waveform modulations, since the modulations have no contribution to the interferometry phase.

1. INTRODUCTION

Synthetic Aperture Radar (SAR) has drawn much attentions of the remote sensing community during the past fifty years [1–4]. Extended from its basic function of two-dimensional imaging, many branches of SAR family have enabled new functions for remote sensing applications, e.g., Polarimetric SAR (PolSAR) [5], multiband SAR [6], bistatic SAR [7, 8], Multi-Input Multi-Output SAR (MIMO SAR) [9], circular SAR [10], and Interferometry SAR (InSAR). Obviously, many techniques concerning SAR are still being developed nowadays [11–13] and will become mature in future.

Received 21 February 2012, Accepted 6 April 2012, Scheduled 26 April 2012

* Corresponding author: Qingfu Liu (liu_675675@163.com).

A Coherent Transponder (CT) was developed long time ago [14, 15] and can serve dual purposes in the area of SAR. One of them is for the calibration of SAR system, such as an active transponder [16, 17]. The other is for the destruction of SAR imaging, such as a coherent jammer. As illustrated in [18], SAR CT is widely utilized for Electronic Counter Measures (ECM), since it has the ability to forge false and verisimilar targets in SAR images and can obtain the processing gain of SAR pulse compression [18]. Although the performances of CT have now been well studied in SAR 2-D imaging and Interferometry SAR (InSAR) has achieved a good state of art in this decade [19, 20], some properties of CT are still unclear in InSAR Digital Elevation Model (DEM).

Considering the coherence between jamming and SAR transmitted signal, SAR ECM can be divided into three categories [18]: the incoherent jamming [21, 22], partially coherent jamming [23, 24], and coherent jamming [18, 25]. From this point of view, CT falls into the third category of SAR ECM. In fact, if the jamming can be detected by SAR, it can be canceled through a number of Electronic Counter-Counter Measures (ECCM) techniques [26], e.g., the wideband sidelobe-cancellation [27], spatial filtering [28], and adaptive beamforming [29]. Although CT has the least probability to be detected by a traditional SAR, it may still be detected by InSAR through the analysis of its DEM and may also be defeated by SAR ECCM techniques mentioned above. This is also an important impetus for us to study the properties of CT in deeper depth.

Upon our earlier research presented in [26], the interferometry phase of CT with arbitrary waveform modulations has been proved to be a constant for both single-pass and repeat-pass InSAR working modes. To continue the work of [26], we mainly focus on the DEM properties of CT in this paper and try to illustrate the differences between DEMs forged by CT and that formed by natural terrain. The rest of the paper is organized as follows. Section 2 discusses the slant-range frequency spectrum and the quality map of CT. Section 3 presents the DEM "slope" effect of CT. Section 4 gives the simulations of "slope" effect. Section 5 gives the conclusion.

2. THE QUALITY MAP OF CT

There are four popular quality maps for InSAR: correlation map, pseudo-correlation map, phase-derivative-variance map, and maximum-phase-gradient map [30]. The correlation map is important because it is the best estimator for the quality of the phase data extracted from InSAR data [31, 32]. For both path-following and

minimum-norm phase unwrapping methods, correlation map can be utilized to improve the unwrapping performances. Under the considerations mentioned above, only correlation map of CT is discussed in this section.

The two-dimensional frequency spectrum of CT in InSAR's two channels can be expressed as [26]

$$\begin{cases} G_m(f_r, f_a) = \tilde{G}(f_r, f_a) \exp\{-j\Phi_m\} \\ G_s(f_r, f_a) = \tilde{G}(f_r, f_a) \exp\{-j\Phi_s\} \end{cases} \tag{1}$$

where both the subscripts "m" and "s" represent master channel and slave channel of InSAR system; f_r and f_a are fast-time frequency and Doppler frequency; $j = \sqrt{-1}$, $\tilde{G}(f_r, f_a)$ is a function determined by CT's waveform modulation.

$$\begin{aligned} \tilde{G}(f_r, f_a) \;=\; & G\left(\sqrt{(f_c + f_r)^2 + \frac{c^2 f_a^2}{4v_a^2}} - f_c, f_a\right) \\ & \times \exp\left\{-j\frac{\pi}{K_r}\left[\sqrt{(f_c + f_r)^2 + \frac{c^2 f_a^2}{4v_a^2}} - f_c\right]^2\right\} \end{aligned} \tag{2}$$

f_c is the carrier frequency of SAR transmitted signal, v_a the velocity of SAR platform, c the velocity of light, and K_r the chirp rate.

$$\Phi_m \;=\; \frac{4\pi(R_m - R_{ref})}{c}(f_c + f_r) \tag{3}$$

$$\Phi_s \;=\; \begin{cases} \dfrac{4\pi[0.5(R_m + R_s) - R_{ref}]}{c}(f_c + f_r) & \text{single-pass} \\ \dfrac{4\pi(R_s - R_{ref})}{c}(f_c + f_r) & \text{repeat-pass} \end{cases} \tag{4}$$

R_m is the minimum slant range between the master antenna's phase center and the transponder's transmit antenna phase center. R_s is the minimum slant-range between the slave antenna phase center and the transponder's transmit antenna phase center. R_{ref} is the reference slant-range of InSAR imaging scene center.

The relationship between the two-dimensional frequency spectrums of InSAR's two channels can be deduced from (1) as

$$G_m(f_r, f_a) = G_s(f_r, f_a) \exp\{-j\Delta\Phi\} \tag{5}$$

where

$$\Delta\Phi = \begin{cases} \dfrac{2\pi(R_m - R_s)}{c}(f_c + f_r) & \text{single-pass} \\ \dfrac{4\pi(R_m - R_s)}{c}(f_c + f_r) & \text{repeat-pass} \end{cases} \tag{6}$$

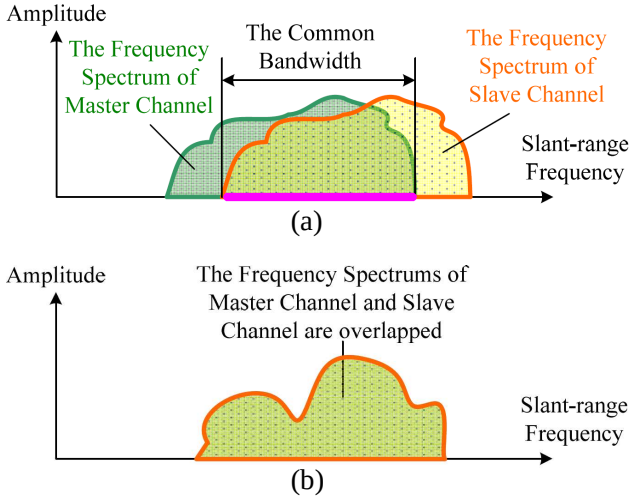

Figure 1. The frequency spectrums in InSAR's two channels. (a) The slant-range frequency spectrums of natural terrain in InSAR's two channels. (b) The slant-range frequency spectrums of CT in InSAR's two channels.

It can be seen from (5) that there exists only a phase shift between the two channels' frequency spectrums. For repeat-pass InSAR working mode, this conclusion is also true except that the phase difference in (5) is now changed twice. Therefore, CT's two-dimensional frequency spectrums in the two channels of InSAR are overlapped with each other. This phenomenon is quite different from that of natural terrain of which the two-dimensional frequency spectrums are shifted proportionally to InSAR baseline length in slant-range direction (as shown in Fig. 1). From this point of view, the coherency of CT is higher than that of natural terrain for InSAR's two channels, because decorrelation happens in the imaging results of natural terrain in InSAR's two channels but not in that of CT.

Also, the coherence of CT's interferogram can be understood for the definition of correlation coefficient. The correlation coefficient of CT in InSAR's two channels can be expressed in the discrete form as

$$\chi = \frac{\sum g_m(i,j)\, g_s^*(i,j)}{\sqrt{\sum |g_m(i,j)|^2 \sum |g_s(i,j)|^2}} \tag{7}$$

where i and j denote the indexes of pixels in slant-range direction and azimuth-range direction, respectively. $(\cdot)^*$ denotes complex conjugate. $g_m(i,j)$ and $g_s(i,j)$ are the imaging results of master channel and

slave channel after InSAR image registration, respectively.

The Schwarz inequality states that

$$\left|\sum g_m(i,j)\, g_s^*(i,j)\right| \le \left|\sqrt{\sum |g_m(i,j)|^2 \sum |g_s(i,j)|^2}\right| \tag{8}$$

So the magnitude of χ (i.e., $|\chi|$) has never been greater than one in value. Equality in (8) holds if and only if

$$g_m(i,j) = C \cdot g_s(i,j) \tag{9}$$

where C is a complex constant. Note that g_m and g_s are the Inverse Fourier Transform (IFT) of G_m and G_s after the image registration of InSAR, but not merely the IFT of them [26]. As demonstrated by [26], the relationship between g_m and g_s can be written as

$$g_m(i,j) = g_s(i,j) \exp\{-j\theta\} \tag{10}$$

where

$$\theta = \begin{cases} \dfrac{2\pi(R_m - R_s)}{c} f_c & \text{single-pass} \\ \dfrac{4\pi(R_m - R_s)}{c} f_c & \text{repeat-pass} \end{cases} \tag{11}$$

Comparing (9) and (10), we obtain

$$C = \exp\{-j\theta\} \tag{12}$$

i.e., the correlation coefficient of CT's interferogram is of unity magnitude. For natural terrain, the magnitude of correlation coefficient is usually smaller than one, also smaller than that of CT. Although the flat earth phase is removed from InSAR interferogram before the phase unwrapping process, the relationship presented in (10) also holds true for phase unwrapping, due to the usage of the same flat earth phase for InSAR's two channels. Therefore, good quality map would be expected for CT's interferogram, so long as the transmit power of CT is big enough to suppress the echo from its background terrain. However, the correlation coefficient will decrease in the intersection region of CT and natural terrain, and this can be further pursued as follows. In the region of high Jamming-to-Clutter power Ratio (JCR), the interferometry phase of InSAR interferogram is determined by CT (as shown in Fig. 2). On the contrary, the interferometry phase of InSAR interferogram is determined by natural terrain in the region of low JCR. If JCR changes dramatically in the intersection region of CT and natural terrain, the interferometry phase of InSAR interferogram may also be changed prominently. This phenomenon implies that the coherence of InSAR interferogram will decrease in the intersection region.

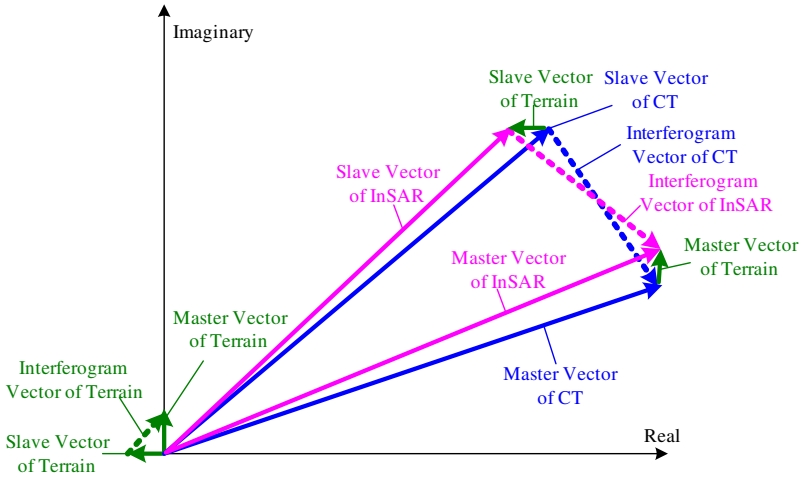

Figure 2. InSAR interferogram in high JCR region.

3. THE "SLOPE" EFFECT OF CT'S DEM

As elucidated by [26], if a CT has only a single transmit antenna, the interferometry phase of its transmitted signal will be a constant, equal to the interferometry phase of the terrain where the CT lies in. Since the CT and its transmit signal has the same interferometry phase, they will have the same wave number difference with respect to InSAR's two channels, i.e., they should have the same slant range difference with respect to the master and slave channels. Also, InSAR interferometry phase will remain unchanged along the across-range direction if changes do not happen in vertical direction or ground-range direction. This means that the DEM of CT will be independent of the across-range direction. Upon this consideration, only the two-dimensional coordinates consisting of the ground-range direction and the vertical direction are considered in the following, which are denoted as the Y-O-Z coordinates in Fig. 3. Both the InSAR baseline and the transponder are assumed to be in the Y-O-Z plane in Fig. 3, namely,

$$x_m = x_s = x_t = 0 \tag{13}$$

where x_m, x_s and x_t denote the across-range direction coordinates of the antenna phase center with respect to InSAR's two channels and the CT, respectively. Also, the coordinates corresponding to x_m, x_s and x_t in the other two directions can be denoted as $\{y_m, z_m\}$, $\{y_s, z_s\}$,

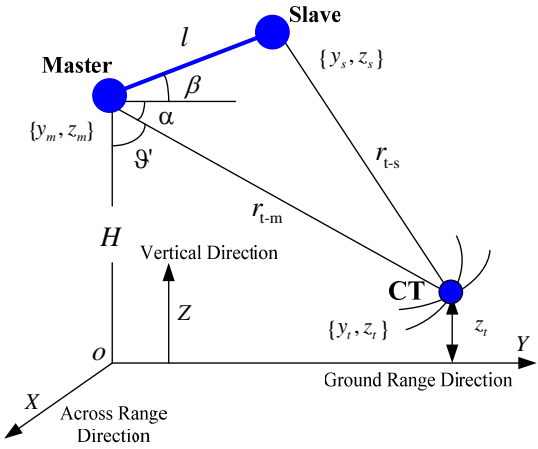

Figure 3. The geometric positions of the coherent transmitter and InSAR baseline.

and $\{y_t, z_t\}$, respectively. From Fig. 3, it can be seen that

$$\begin{cases} y_m = 0 \\ z_s = z_m + h_s \end{cases} \tag{14}$$

where h_s is the length of InSAR baseline in vertical direction. Also, the slant range between the transponder and the master channel can be written as

$$r_{t-m} = \sqrt{y_t^2 + (z_m - z_t)^2} \tag{15}$$

Similarly, the slant range between the transponder and the slave channel can be written as

$$r_{t-s} = \sqrt{(y_t - y_s)^2 + (z_m - z_t + h_s)^2} \tag{16}$$

The slant range difference between r_{t-m} in (15) and r_{t-s} in (16) is

$$\begin{aligned} \Delta r_{t-ms} &= r_{t-m} - r_{t-s} \\ &= \sqrt{y_t^2 + (z_m - z_t)^2} - \sqrt{(y_t - y_s)^2 + (z_m - z_t + h_s)^2} \end{aligned} \tag{17}$$

If the coordinates of the jamming in the Y-O-Z plane are denoted as $\{y, z\}$, then its slant range difference with respect to the InSAR's two channels can be written as

$$\Delta r_{ms}(y, z) = \sqrt{y^2 + (z_m - z)^2} - \sqrt{(y - y_s)^2 + (z_m - z + h_s)^2} \tag{18}$$

As mentioned previously, the slant range differences with respect to InSAR's two channels are equal to each other for both the CT

induced DEM and the terrain where CT lies in, namely, $\Delta r_{ms}(y,z)$ in (18) is equal to Δr_{t-ms} in (17).

$$\Delta r_{ms}(y,z) = \Delta r_{t-ms} \tag{19}$$

In fact, (19) is a hyperbolic function with independent-variables of x and y (i.e., the CT's coordinates in the Y-O-Z plane). Since the jammer is usually far away from InSAR and the baseline length of InSAR relatively short, the hyperbolic function at the position of CT (i.e., the coordinates of $\{y_t, z_t\}$) can be approximated by the Taylor series expansion linearization. By neglecting the second and higher order terms, the two-dimensional Taylor expansion of $\Delta r_{ms}(y,z)$ at the point of $\{y_t, z_t\}$ can be expressed as

$$\begin{aligned}\Delta r_{ms}(y,z) \approx{}& \sqrt{y_t^2 + (z_m - z_t)^2} - \sqrt{(y_t - y_s)^2 + (z_m - z_t + h_s)^2} \\ &+ \left[\frac{y_t}{\sqrt{y_t^2 + (z_m - z_t)^2}} - \frac{y_t - y_s}{\sqrt{(y_t - y_s)^2 + (z_m - z_t + h_s)^2}}\right](y - y_t) \\ &+ \left[\frac{z_t - z_m}{\sqrt{y_t^2 + (z_m - z_t)^2}} - \frac{z_t - z_m - h_s}{\sqrt{(y_t - y_s)^2 + (z_m - z_t + h_s)^2}}\right](z - z_t)\end{aligned} \tag{20}$$

By combining (17), (19) and (20), we obtian

$$\begin{aligned}&\left[\frac{z_t - z_m}{\sqrt{y_t^2 + (z_m - z_t)^2}} - \frac{z_t - z_m - h_s}{\sqrt{(y_t - y_s)^2 + (z_m - z_t + h_s)^2}}\right](z - z_t) \\ \approx{}& -\left[\frac{y_t}{\sqrt{y_t^2 + (z_m - z_t)^2}} - \frac{y_t - y_s}{\sqrt{(y_t - y_s)^2 + (z_m - z_t + h_s)^2}}\right](y - y_t)\end{aligned} \tag{21}$$

Then (21) can be rewritten in a more concise form

$$z - z_t \approx -\frac{y_s - y_t r_{t-m}^{-1} \Delta r_{t-ms}}{h_s + (z_m - z_t) r_{t-m}^{-1} \Delta r_{t-ms}}(y - y_t) \tag{22}$$

As shown in Fig. 3, we can obtain the following relationships

$$\begin{cases} y_t r_{t-m}^{-1} = \sin\vartheta' \\ (z_m - z_t) r_{t-m}^{-1} = \cos\vartheta' \end{cases} \tag{23}$$

where ϑ' is the complementary angle of InSAR's depression angle. And

$$\begin{cases} y_s = l\cos\beta \\ h_s = l\sin\beta \\ \Delta r_{t-ms} \approx l\cos(\beta + \pi/2 - \vartheta') = l\sin(\vartheta' - \beta) \end{cases} \tag{24}$$

where l and β are the length and incline angle of InSAR baseline, respectively. Substituting (23) and (24) into (22) yields

$$z - z_t \approx -\frac{l\cos\beta - l\sin(\vartheta' - \beta)\sin\vartheta'}{l\sin\beta + l\sin(\vartheta' - \beta)\cos\vartheta'}(y - y_t) \tag{25}$$

For the case of $\vartheta' - \beta = \frac{\pi}{2}$, the InSAR's line of sight will be above the horizontal direction, and the terrain cannot be imaged by InSAR. For the case of $\vartheta' - \beta = -\frac{\pi}{2}$, the incline angle of InSAR baseline will be bigger than $\frac{\pi}{2}$. Therefore, the inequality of $\vartheta' - \beta \neq \pm\frac{\pi}{2}$ would hold true for most of the InSAR systems. And the fraction in the right side of (25) can be expressed as

$$\frac{l\cos\beta - l\sin(\vartheta' - \beta)\sin\vartheta'}{l\sin\beta + l\sin(\vartheta' - \beta)\cos\vartheta'} = \cot\vartheta' \tag{26}$$

Substituting (26) into (25) yields

$$z - z_t \approx -\cot\vartheta' \cdot (y - y_t) = -\tan\alpha \cdot (y - y_t) \tag{27}$$

where α is the depression angle of InSAR. Since the interferometry phase of CT is a constant and independent of the across-range direction (namely, the x axis in Fig. 3), its distribution in InSAR DEM will also be irrelevant to the across-range direction. Thus, it can be deduced from (27) that the jamming is distributed within a slant plane, and the incline angle of the slant plane is equal to the supplementary angle of InSAR's depression angle α.

As discussed in Section 2, the quality map in the intersection region of CT and natural terrain will decrease, if JCR varies dramatically in the region. This will induce residues in this region where the interferometry phase difference between CT and natural terrain is relatively big. For both path-following and least-norm phase unwrapping algorithms, the residues in the intersection region will introduce "shear" or boundaries of discontinuities between two regions (i.e., high JCR region and low JCR region).

Since the interferometry phase derived from InSAR interferogram is "wrapped", the interferometry phases with equal value in InSAR interferogram are not necessary corresponding to an equal slant-range difference (as shown in Fig. 4). So (19) can be extended to

$$W\left\{2\pi\frac{\Delta r_{ms}(x,y)}{\lambda}\right\} = W\left\{2\pi\frac{\Delta r_{j-ms}}{\lambda} + 2k\pi\right\} \tag{28}$$

where W defines a wrapping operator, $k = 0, \pm1, \pm2, \ldots$, λ is the carrier wavelength. Obviously, (28) is a necessary but not sufficient

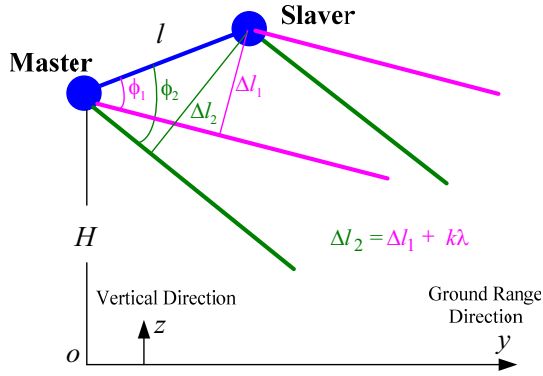

Figure 4. Different depression angle may share the same wrapped interferometry phase.

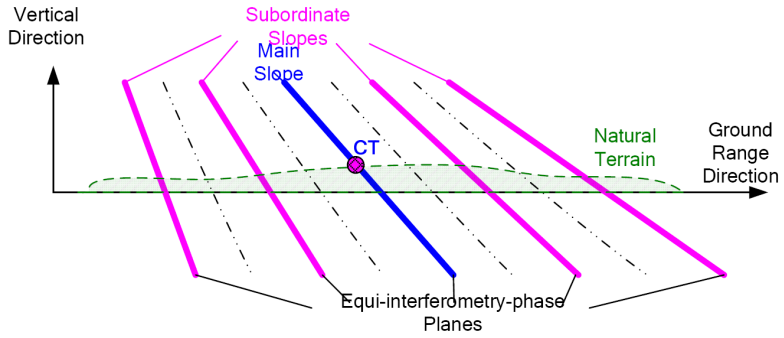

Figure 5. Multi-slope effect for the DEM of CT.

condition of (19). Combining (17), (20), and (28) yields

$$\left[\frac{z_t - z_m}{\sqrt{y_t^2 + (z_m - z_t)^2}} - \frac{z_t - z_m - h_s}{\sqrt{(y_t - y_s)^2 + (z_m - z_t + h_s)^2}}\right](z - z_t) + k\lambda$$
$$\approx \left[\frac{y_t}{\sqrt{y_t^2 + (z_m - z_t)^2}} - \frac{y_t - y_s}{\sqrt{(y_t - y_s)^2 + (z_m - z_t + h_s)^2}}\right](y - y_t) \quad (29)$$

Then (21) can be rewritten in a more concise form

$$(z - z_t) + \gamma_c k\lambda \approx -\frac{y_s - y_t r_{t-m}^{-1} \Delta r_{t-ms}}{h_s + (z_m - z_t)\, r_{t-m}^{-1} \Delta r_{t-ms}} (y - y_t) \quad (30)$$

where

$$\gamma_c = \frac{r_{t-m} r_{t-s}}{(z_t - z_m)\, r_{t-s} - (z_t - z_m - h_s)\, r_{t-m}} = \frac{r_{t-m} r_{t-s}}{\Delta r_{t-ms}\,(z_m - z_t) + h_s r_{t-m}} \tag{31}$$

Substituting (23) and (24) into (30) and after some manipulations yields

$$z - z_k \approx -\tan\tilde{\alpha} \cdot (y - y_k) \tag{32}$$

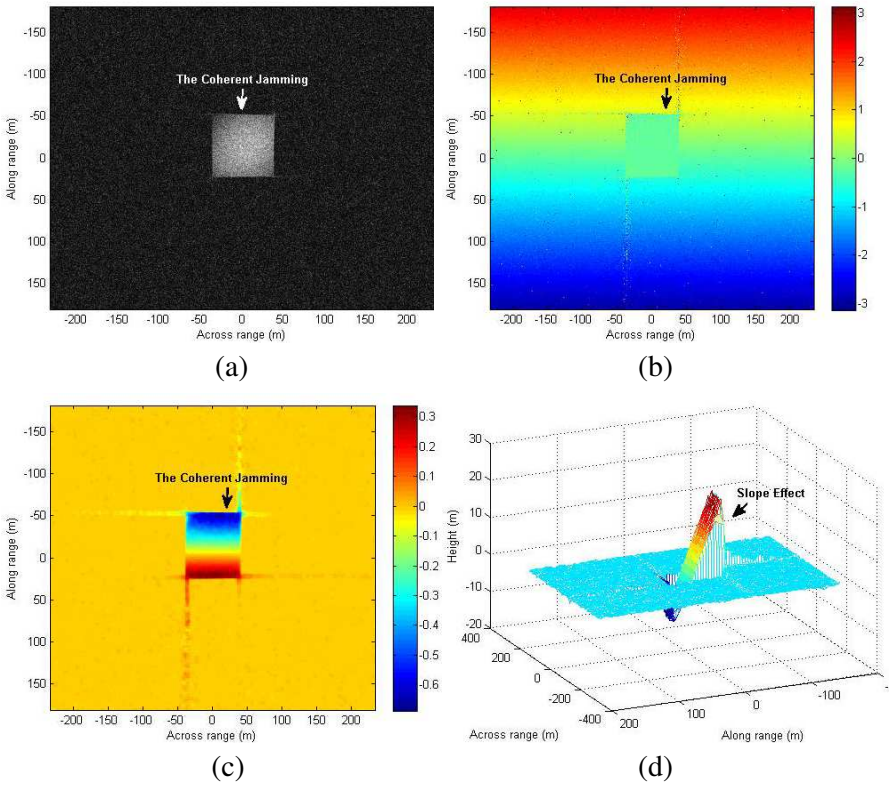

Figure 6. Scenario I: The InSAR processing results of CT and the "slope" effect (the baseline length is 2 m, the depression angle is 30 deg, the baseline incline angle is 60 deg). (a) The 2-D image of master channel. (b) The interferometry phase. (c) The phase-unwrapped interferometry phase. (d) The InSAR DEM (the slope's incline angle is 150 deg).

where $\tilde{\alpha}$ must satisfy the following constraint

$$\tilde{\alpha} = \arcsin\left[\sin(\alpha+\beta) + k\frac{\lambda}{l}\right] - \beta \tag{33}$$

l is the baseline length of InSAR.

Therefore, the DEM of CT can be distributed within multiple slant planes, whereas its incline angle of each plane would be different from that presented in (27). If $k = 0$, (33) is reduced to (27), and the slope is called main slope (as shown in Fig. 5). If $k \neq 0$, the incline angle presented in (33) is different from that in (27), and those slopes are called subordinate slopes (as shown in Fig. 5). The phenomenon presented in Fig. 5 is called "multi-slope" effect of CT in InSAR DEM.

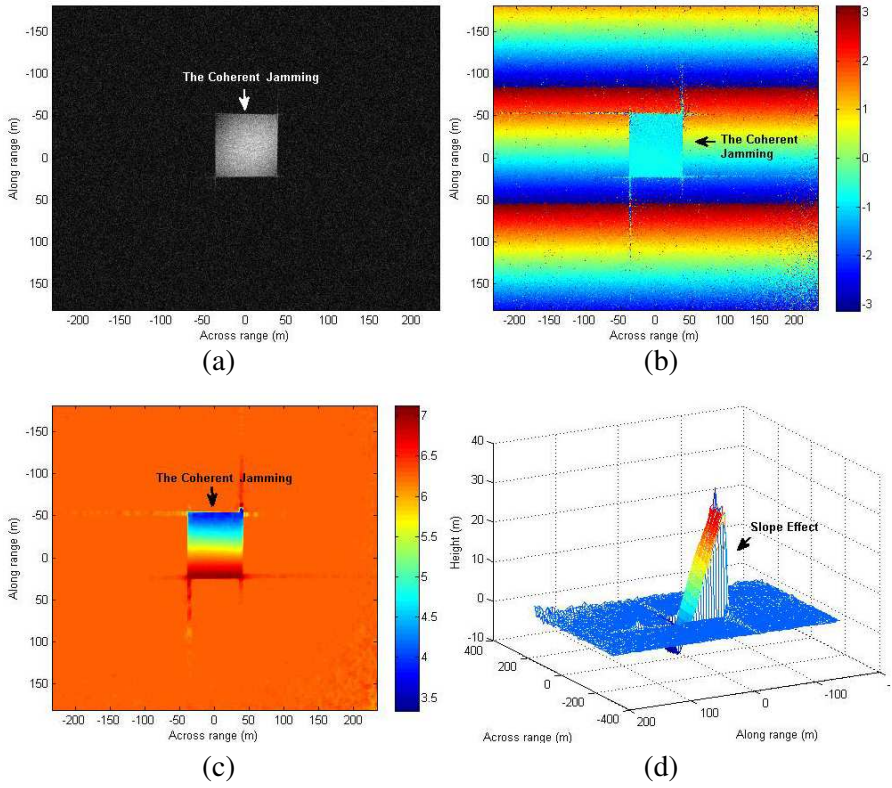

Figure 7. Scenario II: the InSAR processing results of CT and the "slope" effect (the baseline length is changed to 6 m). (a) The 2-D image of master channel. (b) The interferometry phase. (c) The phase-unwrapped interferometry phase. (d) The InSAR DEM (the slope's incline angle is 150 deg).

4. SIMULATION AND ANALYSIS

In order to analyze the distribution of the DEM induced by CT, a 10 dB JCR (the CT's transmitted signal is deemed as jamming here), is set in the following simulation scenarios from I to V. Scenario I is presented as the reference scenario in the simulation, and its parameters are set as follows. The baseline length of InSAR is 2 m; the vertical height of InSAR master channel is 8 km; the depression angle and the incline angle of InSAR baseline are 30 deg and 60 deg, respectively. The terrain, determining the background clutter, is a flat plane with an area of 500 m × 500 m in both the ground-range and azimuth directions.

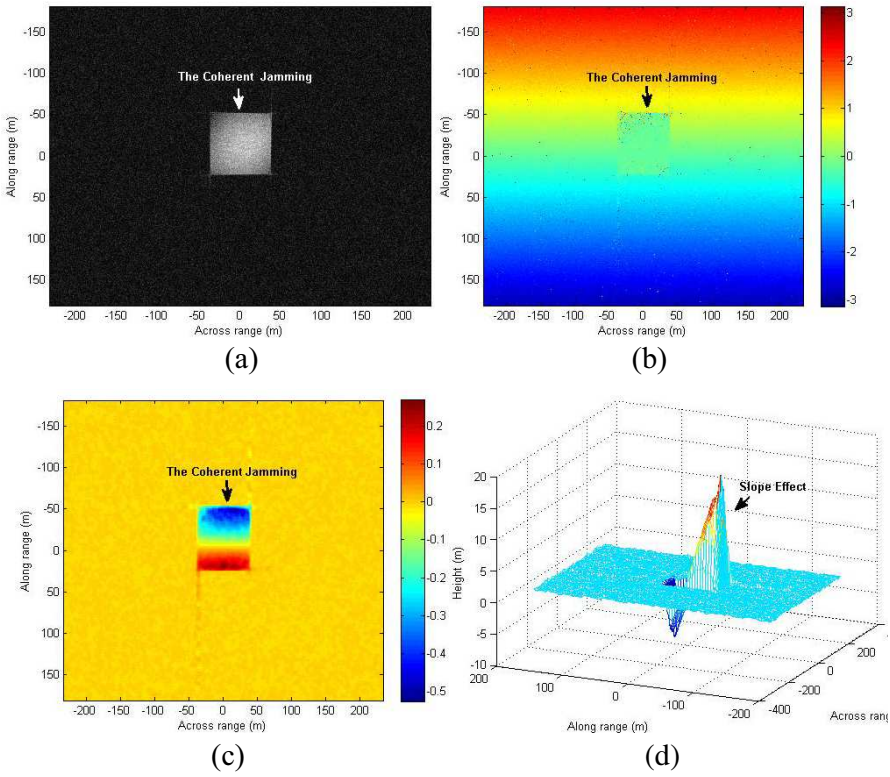

Figure 8. Scenario III: The InSAR processing results of CT and the "slope" effect (the baseline incline angle is changed to 45 deg). (a) The 2-D image of master channel. (b) The interferometry phase. (c) The phase-unwrapped interferometry phase. (d) The InSAR DEM (the slope's incline angle is 150 deg).

The axes scale in the following figures is adjusted in accordance with the imaging scene. The CT lies in a position with −15 m offset from the center of the terrain in the ground-range direction. The frequency-shift modulation [18] is utilized by the CT to produce a rectangular block in InSAR images.

Scenarios II to IV share the same set of parameters with scenario I except that the baseline length in scenario II is 6 m; the incline angle of InSAR baseline in scenario III is 45 deg; the depression angle and the incline angle of the baseline in scenario IV are 60 deg and 30 deg, respectively.

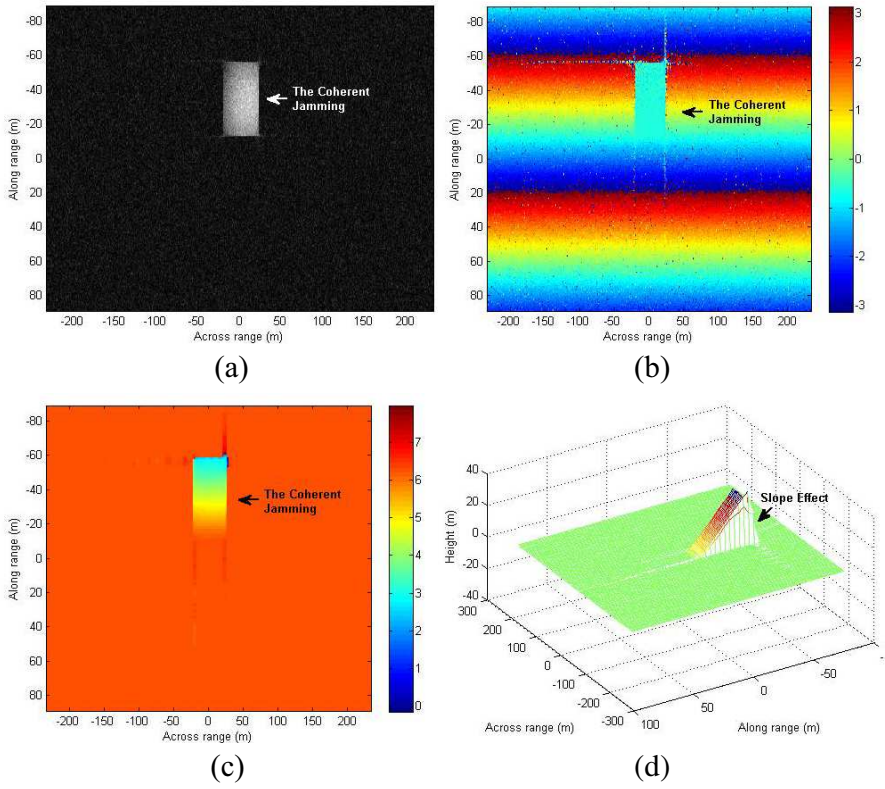

Figure 9. Scenario IV: The InSAR processing results of CT and the "slope" effect (the baseline depression angle is changed to 60 deg, the baseline incline angle is changed to 30 deg). (a) The 2-D image of master channel. (b) The interferometry phase. (c) The phase-unwrapped interferometry phase. (d) The InSAR DEM (the slope's incline angle is 120 deg).

From the subplot (b) of Fig. 6 to Fig. 9, it can be seen that the interferometry phase within the rectangular blocks is a constant determined by the interferometry phase of CT. After removing the flat earth phase, a phase opposite to the flat earth is added upon the rectangle blocks. By comparing the subplot (c) of Fig. 6 to Fig. 9, it can be seen that unwrapped phases within the rectangular blocks are different from each other in different scenarios. However, the "slope" effect can be seen in all of the 3-D images (shown in the subplot (d) of Fig. 6 to Fig. 9). By converting the slant range scale of InSAR 3-D image into the ground range scale, the slant angle of the "slope" can then be calculated, and it is totally determined by the depression angle of InSAR, e.g., the incline angles of scenarios I, II, III are all approximately equal to 150 deg, corresponding to a 30 deg InSAR depression angle; the incline angle of scenario IV is approximately equal to 120 deg, corresponding to a 60 deg InSAR depression angle. Therefore, the incline angle of the "main slope" is determined by the InSAR depression angle and independent of the other parameters of

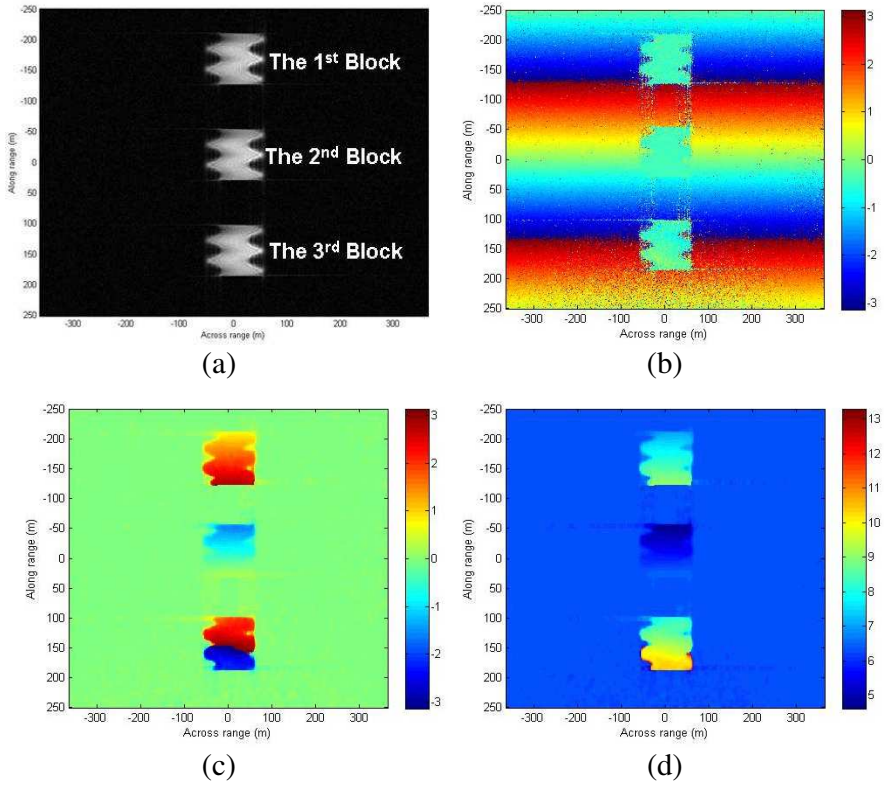

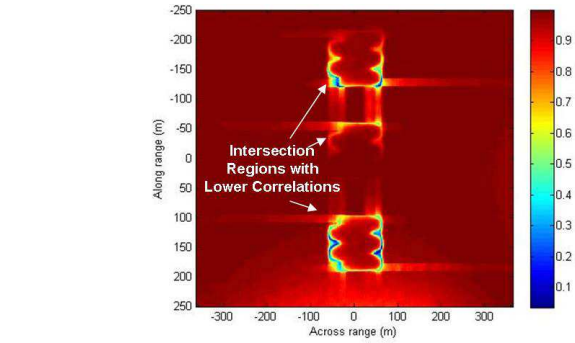

(e)

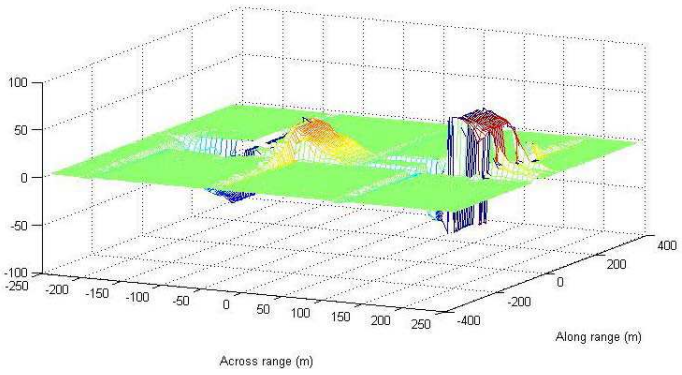

(f)

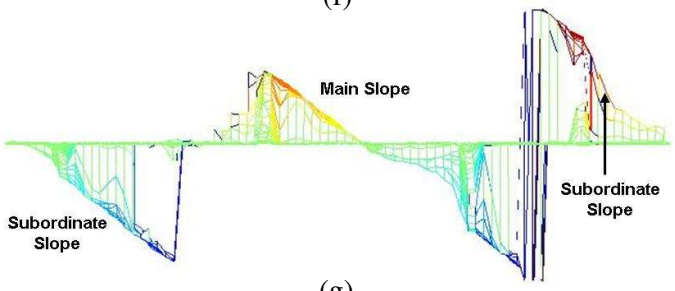

(g)

Figure 10. Scenario V: The InSAR processing results of CT with "multi-slope" effect. (a) The 2-D image of master channel. (b) The interferometry phase. (c) The phase-unwrapped interferometry phase. (d) The InSAR DEM. (e) The correlation coefficients. (f) An overview of InSAR DEM. (g) The side-looking of InSAR DEM (multi-slope effect).

InSAR, e.g., the baseline's incline angle, the baseline's length. Also, the waveform modulation of the CT can only affect the distribution of the "slope" but will not influence its incline angle.

To illustrate the phenomenon of "multi-slope" effect of CT in InSAR DEM, both the depression angle and incline angle of InSAR baseline are assigned to be 45 deg in the simulations of scenario V. From Fig. 10(e), the decorrelation effect in the intersection regions of CT and natural terrain is quite obvious. Note that the decorrelation effects are more prominent for those azimuth-range bins where the interferometry phase differences between natural terrain and CT are large. If there exists no interferometry phase difference, the decorrelation effect will not happen in that azimuth-range bin (e.g., the azimuth-range bin of CT). The "multi-slope" effect in DEM can be seen in the side-looking picture shown in Fig. 10(g). The incline angles of different slopes are different from each other, which are in accordance with our analysis in (33). It is obvious that "slope" effect is an unique characteristic of DEM induced by CT.

5. CONCLUSION

The DEM of CT is consisted of "slopes", if only one transmit antenna is mounted by CT. This is a major difference between the DEMs of natural terrain and that of CT. The incline angle of "main slope" is equal to the supplementary angle of InSAR's depression angle and independent of the other parameters of InSAR system. However, the incline angles of the "subordinate slopes" are determined not only by the depression angle, but also by the baseline length, wavelength, and incline angle of InSAR. Since the interferometry phase of CT is independent of its waveform modulations, all the incline angles of the "slopes" are also irrelevant to the waveform modulations.

REFERENCES

1. Zhao, Y. W., M. Zhang, and H. Chen, "An efficient ocean SAR raw signal simulation by employing fast fourier transform," *Journal of Electromagnetic Waves and Applications*, Vol. 24, No. 16, 2273–2284, 2010.
2. Wei, S.-J., X.-L. Zhang, J. Shi, and G. Xiang, "Sparse reconstruction for SAR imaging based on compressed sensing," *Progress In Electromagnetics Research*, Vol. 109, 63–81, 2010.
3. Park, S.-H., M.-G. Joo, and K.-T. Kim, "Construction of ISAR training database for automatic target recognition," *Journal of*

Electromagnetic Waves and Applications, Vol. 25, No. 11/12, 1493–1503, 2011.

4. Xu, W. and Y. K. Deng, "Investigation on electronic azimuth beam steering in the spaceborne SAR imaging modes," *Journal of Electromagnetic Waves and Applications*, Vol. 25, No. 14/15, 2076–2088, 2011.
5. Jin, Y.-Q., "Polarimetric scattering modeling and information retrieval of SAR remote sensing — A review of fdu work," *Progress In Electromagnetics Research*, Vol. 104, 333–384, 2010.
6. Teng, H. T., H.-T. Ewe, and S. L. Tan, "Multifractal dimension and its geometrical terrain properties for classification of multi-band multi-polarized SAR image," *Progress In Electromagnetics Research*, Vol. 104, 221–237, 2010.
7. Dai, C. and X.-L. Zhang, "Omega-K algorithm for bistatic SAR with arbitrary geometry configuration," *Journal of Electromagnetic Waves and Applications*, Vol. 25, No. 11/12, 1564–1576, 2011.
8. Sun, J., S. Mao, G. Wang, and W. Hong, "Polar format algorithm for spotlight bistatic SAR with arbitrary geometry configuration," *Progress In Electromagnetics Research*, Vol. 103, 323–338, 2010.
9. Lim, S.-H., C. G. Hwang, S.-Y. Kim, and N.-H. Myung, "Shifting MIMO SAR system for high-resolution wide-swath imaging," *Journal of Electromagnetic Waves and Applications*, Vol. 25, No. 8/9, 1168–1178, 2011.
10. Mohammadpoor, M., R. S. A. Raja Abdullah, A. Ismail, and A. F. Abas, "A circular synthetic aperture radar for on-the-ground object detection," *Progress In Electromagnetics Research*, Vol. 122, 269–292, 2012.
11. Woo, J.-C., B.-G. Lim, and Y.-S. Kim, "Modification of the recursive sidelobe minimization technique for the range-doppler algorithm of SAR imaging," *Journal of Electromagnetic Waves and Applications*, Vol. 25, No. 13, 1783–1794, 2011.
12. Han, S.-K., H.-T. Kim, S.-H. Park, and K.-T. Kim, "Efficient radar target recognition using a combination of range profile and time-frequency analysis," *Progress In Electromagnetics Research*, Vol. 108, 131–140, 2010.
13. Koo, V. C., Y. K. Chan, V. Gobi, M. Y. Chua, C. H. Lim, C.-S. Lim, C. C. Thum, T. S. Lim, Z. Bin Ahmad, K. A. Mahmood, M. H. Bin Shahid, C. Y. Ang, W. Q. Tan, P. N. Tan, K. S. Yee, W. G. Cheaw, H. S. Boey, A. L. Choo, and B. C. Sew, "A new unmanned aerial vehicle synthetic aperture radar for environmental monitoring," *Progress In Electromagnetics*

Research, Vol. 122, 245–268, 2012.

14. Weiss, M. and P. Berens, "Motion compensation of wideband synthetic aperture radar with a new transponder technique," *IEEE International Geoscience and Remote Sensing Symposium*, Vol. 6, 3649–3651, 2002.
15. Kemp, W. M. and N. M. Martin, "A synthetic aperture radar calibration transponder at C-band," *Record of the IEEE 1990 International Radar Conference*, 81–85, 1990.
16. Yiding, W., "The maximum phase error of a reflected signal in an active coded transponder," *IEEE Geoscience and Remote Sensing Letters*, Vol. 3, No. 1, 150–153, 2006.
17. Mohr, J. J. and S. N. Madsen, "Geometric calibration of ERS satellite SAR images," *IEEE Trans. on Geoscience and Remote Sensing*, Vol. 39, No. 4, 842–850, 2001.
18. Liu, Q. F., S. Q. Xing, W. S. Wang, and J. Dong, "A strip-map SAR coherent jammer structure utilizing periodic modulation technology," *Progress In Electromagnetics Research B*, Vol. 28, 111–128, 2011.
19. Krieger, G., K. P. Hajnsek, et al., "Interferometric synthetic aperture radar (SAR) missions employing formation flying," *Proceeding of IEEE*, Vol. 98, No. 5, 816–843, 2010.
20. Schneider, R. Z., K. P. Papathanassiou, I. Hajnsek, and A. Moreira, "Polarimetric and interferometric characterization of coherent scatterers in urban areas," *IEEE Trans. Geosci. Remote Sens.,* Vol. 44, No. 4, 971–984, 2006.
21. Condley, C. J., "Some system considerations for electronic countermeasures to synthetic aperture radar," *Lee Colloquium on Published*, 811–817, 1991.
22. Dumper, K., P. S. Cooper, et al., "Spaceborne synthetic aperture radar and noise jamming," *Proceedings of IEE Radar*, 411–414, 1997.
23. Wu, X. F., D. H. Dai, and X. S. Wang, "Study on SAR jamming measures," *IET International Conference on Radar Systems*, 176–179, Edinburgh, England, 2007.
24. Wu, X. F., D. H. Dai, X. S. Wang, and H. Z. Lu, "Evaluation of SAR jamming performance," *International Symposium on Microwave, Antenna, Propagation and EMC Technologies for Wireless Communications*, 1476–1479, 2007.
25. Dai, D. H., X. F. Wu, X. S. Wang, and S. P. Xiao, "SAR active-decoys jamming based on DRFM," *IET International Conference on Radar Systems*, 1–4, 2007.

26. Liu, Q., S. Xing, X. Wang, J. Dong, D. Dai, and Y. Li, "The interferometry phase of InSAR coherent jamming with arbitrary waveform modulation," *Progress In Electromagnetics Research*, Vol. 124, 101–118, 2012.
27. Mrstik, V., "Agile-beam synthetic aperture radar opportunities," *IEEE Trans. on AES*, Vol. 34, No. 2, 500–507, 1998.
28. Joachim, H. G., P. B. Ender, R. B. Andreas, et al., "Multi channel SAR/MTI system development at FGAN: From AER to PAMIR," *2002 IEEE International Geoscience and Remote Sensing Symposium*, Vol. 3, 1697–1701, 2002.
29. Andrew, S. P., "An adaptive beamforming technique for countering synthetic aperture radar (SAR) jamming threats," *2007 IEEE Radar Conf.*, 630–634, 2007.
30. Dennis, C. G. and D. P. Mark, *Two-dimensional Phase Unwrapping Theory, Algorithms, and Software*, John Wiley & Sons. Inc., 1998.
31. Jakowatz, C. V., D. E. Wahl, P. H. Eichel, D. C. Ghiglia, and P. A. Thompson, *Spotlight-mode Synthetic Aperture Radar: A Signal Processing Approach*, Kluwer Academic Publishers, Boston, 1996.
32. Roth, M. W., "Phase unwrapping for interferometric SAR by the least-error path," Johns Hopkins University Applied Physics Laboratory Technical Report, Laurel, Maryland, 1995.